

# REVEALING THE MILKY WAY'S HIDDEN CIRCUMGALACTIC MEDIUM WITH THE COS QUASAR DATABASE FOR GALACTIC ABSORPTION LINES

Y. ZHENG<sup>1</sup>, J. E. G. PEEK<sup>2</sup>, M. E. PUTMAN<sup>1</sup>, AND J. K. WERK<sup>3</sup>

<sup>1</sup> Department of Astronomy, Columbia University, New York, NY 10027, USA; yzheng@astro.columbia.edu

<sup>2</sup> Space Telescope Science Institute, 3700 San Martin Dr, Baltimore, MD 21218, USA

<sup>3</sup> Department of Astronomy, University of Washington, Seattle, WA 98195-1580, USA

## Abstract

Every quasar (QSO) spectrum contains absorption-line signatures from the interstellar medium (ISM), disk-halo (D/H) interface, and circumgalactic medium (CGM) of the Milky Way (MW) along its line of sight. We analyze a sample of 119 QSO spectra observed with the Cosmic Origins Spectrograph on board the *Hubble Space Telescope*, and examine the significance of the Si IV absorption at  $|v| < 100$  km s<sup>-1</sup> in the MW's CGM. We build a 3D kinematic model of the D/H interface based on the commonly adopted 1D flat-slab model and compare it with the observed Si IV column density profiles seen toward the QSOs. 113 of the 119 QSO sightlines show a significant column density excess in addition to the Si IV predicted by the 3D D/H model. We incorporate gas inflows, halo lagging, and turbulent broadening in the model and find that the additional kinematics only mildly affect the significance of the Si IV excess. This excess most likely resides in the extended MW's CGM and was previously hidden by the absorption due to the nearby ISM and D/H interface. We conduct an order-of-magnitude calculations for the CGM mass, including the gas hidden at  $|v| < 100$  km s<sup>-1</sup>, and find a total mass of  $\sim 2 \times 10^{10} M_{\odot} \left(\frac{R_{\text{CGM}}}{160 \text{ kpc}}\right)^2$ . Our mass estimate suggests the MW hosts a similarly massive CGM as other  $L^*$  galaxies at low redshifts. In conducting this study, we produced a carefully continuum-normalized spectral dataset, the COS Quasar Database for Galactic Absorption Lines (COS-GAL), which we release to the public. COS-GAL is based on a subset of the HST Spectroscopic Legacy Archive (Peeples et al. 2017), consisting of 403 QSOs observed with G130M and/or G160M gratings. For each of the QSOs, we provide the normalized continuum, individual ion line spectra, and H I 21cm emission lines extracted from the currently available all-sky H I surveys.

**Keywords:** Galaxy: halo - Galaxy: kinematics and dynamics - Galaxy: structure - quasars: absorption lines - techniques: spectroscopic

## 1. INTRODUCTION

The circumgalactic medium (CGM), the massive multiphase plasma that surrounds a galaxy, exists in a mutualistic relationship with its host. The galaxy grows by accreting material from the CGM, while the CGM is enriched, heated, and stirred by the outflows from the galaxy at its core (Putman et al. 2012; Tumlinson et al. 2017). Thus, one can only understand the existence and evolution of galaxies by studying the structure and dynamics of the CGM.

One of the tools proven most useful for studying the CGM of galaxies is absorption-line observations towards either background quasars (QSOs) or stars in the galaxies themselves. The absorption lines are usually found at the wavelengths of the galaxies' rest frames, tracing the cool/hot phase of the CGM with weakly (e.g., Mg II, Si II) or highly ionized metals (e.g., O VI). With

absorption-line techniques, significant evidence has been found for outflows from galaxies (e.g., Martin et al. 2012; Rubin et al. 2012, 2014; Fox et al. 2015; Bordoloi et al. 2017), inflows to galaxies (e.g., Rubin et al. 2012; Zheng et al. 2017; Rubin 2017), and the CGM as a massive, multiphase reservoir (e.g., Stocke et al. 2013; Werk et al. 2014; Prochaska et al. 2017; Keeney et al. 2017).

The Milky Way (MW) provided the first evidence for a gaseous CGM through detections of cool H I high-velocity clouds (HVCs) and a hot corona (Wakker 2004; Fox et al. 2006; Shull et al. 2009; Putman et al. 2012; Wakker et al. 2012; Bordoloi et al. 2017). However, it remains a difficult place to study CGM dynamics and multiphase structure as we observe the MW's CGM from inside of the Galactic disk. High-velocity gas moving at

$|v^1| > 100 \text{ km s}^{-1}$ , inconsistent with the Galactic rotation, can be safely assumed to be associated with a more distant, non-disk component. Neutral gas at intermediate velocities ( $100 \gtrsim |v| \gtrsim 30 \text{ km s}^{-1}$ ) is generally more consistent with a local gas origin (Lenz et al. 2017); however, the origins of ionized gas moving at low and intermediate velocities ( $|v| \leq 100 \text{ km s}^{-1}$ ) is somewhat ambiguous. Typically, the ionized gas at  $|v| \leq 100 \text{ km s}^{-1}$  at high Galactic latitude ( $b \gtrsim 30^\circ$ ) is thought to arise from the MW’s disk-halo (D/H) interface. However, a simulation work by Zheng et al. (2015) shows there may be a significant amount of CGM gas moving at these lower velocities. In addition, observations of  $L^*$  galaxies at low- $z$  by HST/COS suggest a cool photoionized halo mass of  $\sim 10^{10-11} M_\odot$  (Stocke et al. 2013; Werk et al. 2014; Prochaska et al. 2017; Keeney et al. 2017), while mass estimates of the MW’s CGM find values an order of magnitude lower (Lehner & Howk 2011; Putman et al. 2012). This suggests we may be missing some of the CGM gas for the MW.

The CGM interacts with the Galactic disk through the D/H interface. The MW’s D/H interface is the only one that has been broadly observed and studied in detail. Its multiple gas phases, temperature gradient, scale height, and kinematics are among those properties that are of great interest (Putman et al. 2012). The H I layer of the MW’s D/H interface has a thickness of  $\leq 220 \text{ pc}$  at  $R < R_\odot$  and flares dramatically beyond the solar circle (Dickey & Lockman 1990). The ionized gas at different phases occupies different vertical layers beyond the Galactic H I plane, usually modeled as flat slabs with exponential density profiles (e.g., Savage et al. 1997; Savage & Wakker 2009). In general, the cool component ( $\sim 10^4-5 \text{ K}$ , e.g., H $\alpha$ , S II, Si II) extends  $\sim 2 \text{ kpc}$  above the plane (Haffner et al. 2009), while the warm ( $\sim 10^{5-6} \text{ K}$ ; e.g., Si IV, C IV) and hot ( $\geq 10^6 \text{ K}$ ; e.g., O VI) components fill a larger volume with scale heights of  $\sim 3-5 \text{ kpc}$  (Savage et al. 1997; Bowen et al. 2008; Savage & Wakker 2009; Wakker et al. 2012).

In this work, we leverage the HST Spectroscopic Legacy Archive (HSLA; Peebles et al. 2017) to provide a comprehensive view of the MW’s ionized absorbers towards 403 QSOs that have been observed with the COS G130M and/or G160M gratings. We provide for the community carefully analyzed absorption-line profiles in the Galactic reference frame of P II, S II, Fe II, Si II, Si III, Si IV, C II and C IV. We carefully select 119 QSO sightlines with high-quality Si IV doublet to test the standard hypothesis that most low- and intermediate-velocity absorption is generated by the MW’s D/H inter-

face. We do this through a comparison of the observed Si IV profiles to a 3D version of the current popular flat-slab model of the MW’s D/H interface (Savage & Wakker 2009; hereafter SW09).

This paper is organized as follows. § 2 introduces our COS Quasar Database for Galactic Absorption Lines (COS-GAL), a subset retrieved from HSLA, and describes the continuum normalization process and sight-line selection criteria. We release our COS-GAL to the community, and the dataset can be found here: [10.17909/T9N677]. Based on SW09’s 1D flat slab model, in § 3 we build a 3D kinematic model of the MW’s D/H interface and implement co-rotation, halo lagging, and gas inflows. We compare the observed Si IV column density profiles seen towards QSOs with the modeled MW-D/H profiles, and find significant Si IV excess beyond the MW’s D/H interface. In § 4 we discuss the implications of the Si IV excess and conduct an order-of-magnitude estimate for the MW’s CGM mass. We conclude our main results in § 5.

## 2. DATA

### 2.1. The COS Quasar Database for Galactic Absorption Lines

We obtain our QSO spectra from the HSLA (Peebles et al. 2017). The first release of HSLA (February 2017) delivers uniformly reduced and co-added COS/FUV spectra that have been observed with M-mode (medium-resolution gratings, i.e., G130M and G160M) and L-mode (low-resolution grating, i.e., G140L). For each of the targets, the spectra from different programs, epochs, and gratings are co-added to improve the signal-to-noise ratio (SNR) and the wavelength coverage. The HSLA arranges targets into different categories, such as “Solar Systems and Exoplanets”, “Stars” and “Galaxies and Clusters”; in this work, we make use of those spectra under the “QSOs, AGNs, and Seyferts” category, which we will henceforth refer to as the HSLA QSO catalog.

Fig 1 summarizes the criteria we use to refine our dataset from the HSLA QSO catalog. The HSLA provides coadded spectra of 513 QSOs observed with G130M and/or G160M gratings. Each spectrum is characterized by a typical SNR, which is defined as the mean of the SNR values per resolution element (taken to be six pixels) calculated over  $10 \text{ \AA}$  windows every  $1000 \text{ \AA}$  starting from  $1150 \text{ \AA}$  (Peebles et al. 2017). We select those QSOs with a typical  $\text{SNR} \geq 5$  and conduct continuum normalization near the velocity centroid of the lines of interest (§ 2.2). This criterion leaves 403 QSOs with G130M and/or G160M gratings, which form our COS Quasar Database for Galactic Absorption Lines (COS-GAL).

<sup>1</sup> In this work, we use velocity in the rest frame of the local standard of rest unless otherwise specified.

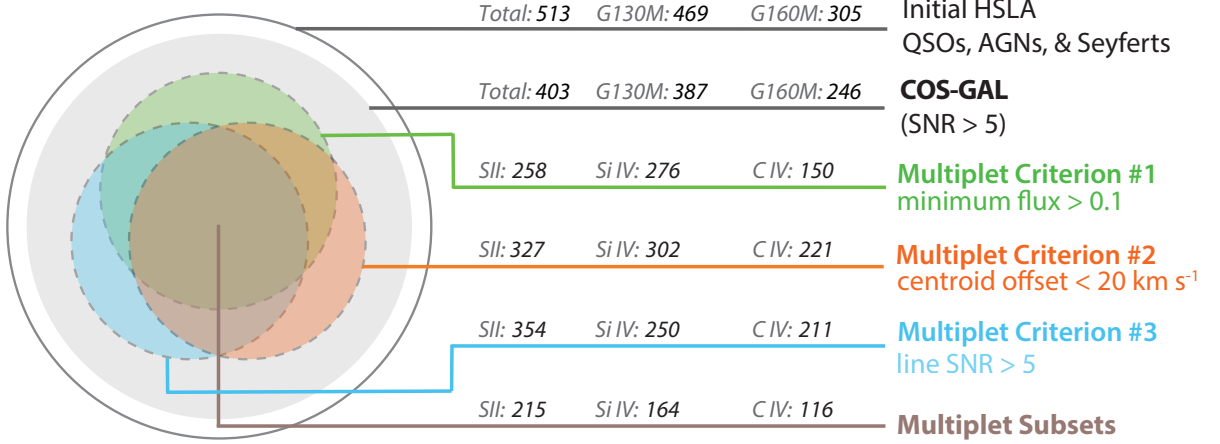


**Figure 1.** The selection criteria used to refine our dataset from the HSLA. We first require a typical SNR  $> 5$  to form our COS Quasar Database for Galactic Absorption Lines (COS-GAL). Then the spectra of all the QSOs in COS-GAL are continuum-normalized (see § 2.2), and are released to the community (see § 2.4); the dataset can be found here: [10.17909/T9N677]. For this work, we use three independent criteria to control the line quality of the S II triplet, Si IV and C IV doublets (see § 2.3).

## 2.2. Continuum Normalization and Individual Line Extraction

For each QSO in our COS-GAL dataset, we perform continuum normalization for a number of lines of interest, including the S II triplet, Si IV and C IV doublets, and P II 1152 Å, Fe II 1142/1143/1144/1608 Å, C II 1334 Å, Si II 1190/1193/1260 Å and Si III 1206 Å transition lines. We use the *Linetools*<sup>2</sup> package to continuum normalize our spectra. Linetools is an in-development open-source 1D spectral analysis package. Its continuum normalization function (*Xspectrum1D.fit\_continuum*<sup>3</sup>) makes use of an Akima Spline to generate the continua for the non-absorption regions.

After the continuum normalization, we extract spectra within  $\pm 1000$  km s<sup>-1</sup> of the rest wavelength of the lines of interest and write the data into fits files. Each fits file includes the original spectral line data, the absorption-line-free continuum, the continuum-normalized flux, and the errors. We release these line fits files and the full QSO spectra to the community; details on the data release can be found in § 2.4. Note that these continuum-normalized spectra are specifically processed to study the absorption lines associated with the ionized gas of the Milky Way. They are not ideal for the studies of any broad features, especially those that are intrinsic to the host QSOs. Users interested in these features should examine the original spectra and continua carefully before using our continuum-normalized spectra.

## 2.3. Multiplet Criteria

In addition to the typical SNR  $\geq 5$  requirement for the COS-GAL (see § 2.1), for this paper we use three independent criteria to highlight the S II<sup>4</sup> (1250/1253/1259 Å), C IV (1548/1550 Å), and Si IV (1391/1402 Å) multiplet subsets (see Fig 1). These three sets of ion multiplets are of particular interest because they trace different gas phases of the interstellar medium (ISM) and CGM. Furthermore, the detection of multiple lines for each ion ensures the existence and measurement of the ion, which may otherwise suffer contamination from miscellaneous lines at higher redshifts that happen to lie at similar wavelengths.

First, the minimum flux of each absorption feature should be  $\geq 0.1$ . Theoretically, an absorption line becomes saturated (optically thick) when its flux reaches 0.0. In the case of COS spectroscopy, it has been empirically found that the spectra become saturated when the flux is below 0.1. This criterion keeps 258/276/150 QSO spectra from COS-GAL for the S II/Si IV/C IV lines, respectively. This is referred to as the Multiplet Criterion #1 in Fig 1.

Second, for each ion, we calculate the flux-weighted centroids within  $\pm 90$  km s<sup>-1</sup> for the multiplet lines and require the difference between the centroid values to be  $\leq 20$  km s<sup>-1</sup>. This criterion effectively excludes contamination from extragalactic absorbers along the QSO paths at certain wavelengths and leaves us with

<sup>2</sup> <https://github.com/linetools/linetools>

<sup>3</sup> <http://linetools.readthedocs.io/en/latest/xspectrum1d.html>

<sup>4</sup> For S II, we use 1250 and 1253 Å for the three multiplet criteria since they are weaker and thus less likely to be saturated than the 1259 line.

327/302/221 QSO spectra from COS-GAL for S II/Si IV/C IV, respectively, shown as Multiplet Criterion #2.

Lastly, for each line of interest, we calculate the line SNR per resolution element (taken to be six pixels for G130M and ten for G160M) and keep only those that have line  $\text{SNR} \geq 5$ . This SNR criterion is different from the typical SNR requirement we previously use to form our COS-GAL; the typical SNR was evaluated by HSLA over the whole wavelength span of the corresponding co-added QSO spectrum. This criterion leaves 354/250/211 QSOs from COS-GAL for S II/Si IV/C IV, respectively, shown as Multiplet Criterion #3 in Fig 1.

Ultimately, we combine Multiplet Criteria #1, #2 and #3 to select a total of 215/164/116 QSO sightlines that form our S II/Si IV/C IV Multiplet Subsets, as shown in Fig 1. The three criteria altogether reduce the uncertainty associated with saturated and/or blended systems while ensuring large enough statistical samples to perform scientific analyses.

#### 2.4. Data Product Release

We release the continuum-normalized QSO spectra as described above to the community, as the COS Quasar Database for Galactic Absorption Lines (COS-GAL). We provide a master table in which the name, coordinates ( $l$ ,  $b$ ), redshift  $z$ , and SNR of each QSO are listed. We provide flags that indicate whether a given QSO meets our Multiplet Criterion #1, #2, or #3 used for this paper (see Fig 1 and § 2.3).

Along with the continuum-normalized lines, we provide H I 21cm emission line spectra at the position of each QSO. We extract the H I 21cm lines from three different surveys: GALFA-H I (Peek et al. 2017), HI4PI (HI4PI Collaboration et al. 2016), and LAB (Kalberla et al. 2005). GALFA-H I covers 32% of the sky with finer spatial and velocity ( $4'/0.18 \text{ km s}^{-1}$ ) resolution, while the other two surveys are for the full Galactic sky but with lower resolution ( $16.2'/1.49 \text{ km s}^{-1}$  for HI4PI and  $36'/1.25 \text{ km s}^{-1}$  for LAB). We refer the reader to Table 1 in HI4PI Collaboration et al. (2016) for a comparison of the three surveys. For each of the QSOs, we extract H I 21cm lines from GALFA-H I averaged over the  $4'$  beam, from HI4PI averaged over the  $16.2'$  beam, and from LAB averaged over the  $36'$  beam and over  $1^\circ$ .

Note that the COS spectra are observed with an aperture size of only  $2.5''$ , which is much smaller than the radio beam sizes of the H I surveys. Thus, we caution that the ionized gas traced by COS-GAL and the neutral gas traced by these HI surveys may not be entirely co-spatial. We provide the HI spectra at various resolutions to partially investigate this and refer the reader to a study by Wakker et al. (2001) that examines the influence of different radio beam sizes on studies of high- and intermediate-velocity clouds.

### 3. THE FIRST APPLICATION OF COS-GAL: A 3D KINEMATIC MODEL OF THE GALACTIC DISK-HALO INTERFACE

As the first application of our COS-GAL dataset, we investigate the Si IV-bearing gas moving at  $|v| < 100 \text{ km s}^{-1}$  in the MW. In § 3.1, we convert Si IV absorption lines into apparent column density profiles and examine the correspondence of the two transitions. The Si IV doublets are chosen because this ion has been widely used in previous MW studies (e.g., Savage et al. 1997; Savage & Wakker 2009; Wakker et al. 2012). In § 3.2, we separate the D/H Si IV signals from the observed QSO profiles by building a 3D D/H kinematic model that is based on SW09's 1D flat slab. In § 3.3, we quantify the significance of the Si IV excess that does not belong to the MW's D/H interface.

#### 3.1. Si IV Apparent Column Density Profile $N_{\text{SiIV}}(v)$

For each of the 164 QSO sightlines in the Si IV doublet subset (Fig 1), we use the apparent optical depth (AOD) method (Savage & Sembach 1991, 1996) to create the apparent column density profiles,  $N_{1393}(v)$  and  $N_{1402}(v)$ . We focus on the spectral region of  $|v| < 400 \text{ km s}^{-1}$  for the MW gas in this study. We visually inspect the  $N_{1393}(v)$  and  $N_{1402}(v)$  profiles and discard a sightline if the two profiles deviate from each other by  $\gtrsim 5 \times 10^{11} \text{ cm}^{-2}$  per  $\text{km s}^{-1}$  over the  $|v| \leq 400 \text{ km s}^{-1}$  region. This additional criterion excludes 45 QSO sightlines; most of the sightlines are discarded due to profile discrepancies at  $100 < |v| < 400 \text{ km s}^{-1}$ , which likely arise from blends with non-Si IV features of intervening, redshifted absorbers. For each of the remaining 119 QSO sightlines, we take the mean of the  $N_{1393}(v)$  and  $N_{1402}(v)$  profiles to generate the Si IV apparent column density profile  $N_{\text{SiIV}}(v)$ . Fig 2 shows the distribution of the 119 QSOs; all the QSOs are at Galactic latitudes of  $|b| \geq 20^\circ$ . We will use the Si IV column density profiles  $N_{\text{SiIV}}(v)$  from these 119 QSOs in the following analyses.

#### 3.2. Building a 3D Kinematic Flat-Slab Model

First, we briefly review the commonly-adopted 1D flat-slab model of the MW's D/H interface, and the best-fit scale height and number density of the Si IV flat slab derived by SW09 (§ 3.2.1). Then we transform SW09's model into a 3D kinematic flat slab and implement co-rotation (§ 3.2.2). Lastly, we incorporate halo lagging, gas inflows, and turbulent broadening in the 3D kinematic model to investigate how different kinematics affect the Si IV column density profiles (§ 3.2.3).

##### 3.2.1. A Brief Review of the 1D Flat-Slab Model

A simple physical scenario envisions the MW's D/H interface as a 1D flat slab with an exponential density profile,  $n(z) = n_0 e^{-|z|/z_h}$ , extending above and be-



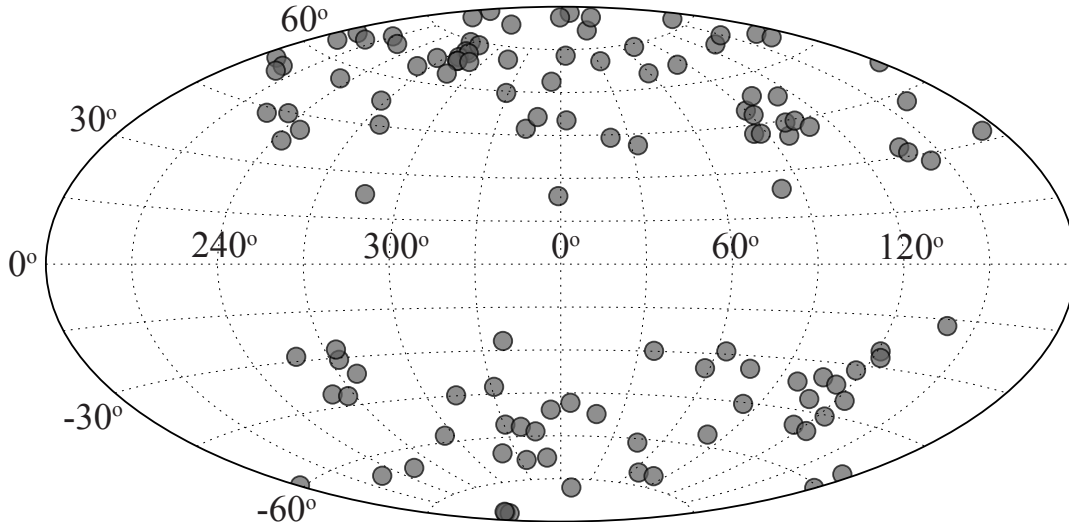


**Figure 2.** Aitoff distribution of the 119 QSOs used in our analysis to study the Si IV content in the MW’s D/H interface as well as its CGM. The QSOs are selected based on Si IV Multiplet Criterion #1, #2, #3 (see Fig 1) and an additional criterion on matching the doublet apparent column density profiles from  $-400$  to  $400$   $\text{km s}^{-1}$  (see § 3.1).

low the Galactic disk. In this equation,  $z$  is the vertical distance from the Galactic plane,  $z_h$  is the scale height, and  $n_0$  is the mid-plane number density.  $z_h$  and  $n_0$  can be constrained by examining ion column density distributions seen towards background halo stars at various distances from the Galactic plane. For a star at height  $z_s$  from the Galactic plane, the modeled column density of an ion X seen towards the star will be  $N_{X,\text{mod}} = \int_0^{z_s} n(z, X) dz$ .  $N_{X,\text{mod}}$  can then be related to the observed column density towards the star as  $N_{X,\text{mod}} = N_{X,\text{obs}} \sin|b|$ , where  $b$  is the star’s Galactic latitude. Since the number density of the flat slab drops dramatically above the scale height  $z_h$ ,  $N_{X,\text{mod}}$  flattens as we probe background stars at vertical distances much larger than  $z_h$ .

To test the flat slab model, SW09 searched the literature and collected the column densities of a number of ions (e.g., H I, Si IV, C IV, O VI) from 109 halo star sightlines and 30 QSO sightlines. The halo stars they used are beyond one kpc, with an average distance of 2.9 kpc. The ion column densities from different sources were integrated over slightly different velocity ranges, but all near  $[-100, 100]$   $\text{km s}^{-1}$ . SW09 examined the trend of  $N_{X,\text{obs}} \sin|b|$  with respect to  $\log|z|$  for different ions. They found  $N_{X,\text{obs}} \sin|b|$  increases with  $\log|z|$  and the relation reaches a plateau at a given  $\log|z|$  value that depends on the ion. They compared this observed  $N_{X,\text{obs}} \sin|b|$ - $\log|z|$  trend with that predicted by the 1D flat slab, and used the comparison to constrain the scale height and mid-plane density of the flat slab’s exponential profile. For Si IV, they found the best-fit parameters to be  $z_h = 3.2^{+1.0}_{-0.6}$  kpc and  $n_0 = 2.3 \times 10^9 \text{ cm}^{-3}$ .

SW09’s 1D flat-slab model successfully explains the

origin of the Si IV column densities seen towards nearby halo stars. One important caveat with this model is that it lacks kinematic information since only the exponential density profile is fit. In § 3.2.2, we build a 3D kinematic version of SW09’s flat slab model to examine the Si IV column density profile for any given sightline through the MW’s D/H interface.

### 3.2.2. A Co-rotating 3D Flat-slab Model

We build a 3D kinematic model for the Si IV-bearing gas at the MW’s D/H interface. Our model is based on the 1D flat-slab parameters  $(n_0, z_h) = (2.3 \times 10^9 \text{ cm}^{-3}, 3.2 \text{ kpc})$  as derived in SW09. We assume a cylindrical shape for the flat slab with an exponential profile along the  $z$  direction. The cylinder is co-rotating with the disk at  $v_{\text{rot}} = 220 \text{ km s}^{-1}$ . We refer to this model as the *rotation-only* model, and in § 3.2.3 we will include additional kinematic signatures – inflows, halo lagging, and turbulent broadening, and address their influences on shaping the Si IV kinematic profiles.

Towards a given line of sight, we compute the Si IV column density distribution as a function of velocity. We convolve the modeled distribution with Gaussian profiles to produce realistic line shapes, assuming the Si IV particles follow a Maxwellian distribution at a thermal temperature of  $8 \times 10^4 \text{ K}$ , which is the temperature at which Si IV ionization fraction reaches its peak under collisional ionization equilibrium at a metallicity of  $Z = 0.1 Z_\odot$  (Gnat & Sternberg 2007). We also include a turbulent broadening term of  $b_{\text{turb}} = 20 \text{ km s}^{-1}$  in the profile convolution. Note that this profile convolution does not change the total amount of Si IV along a given line of sight, which is only determined by the 1D

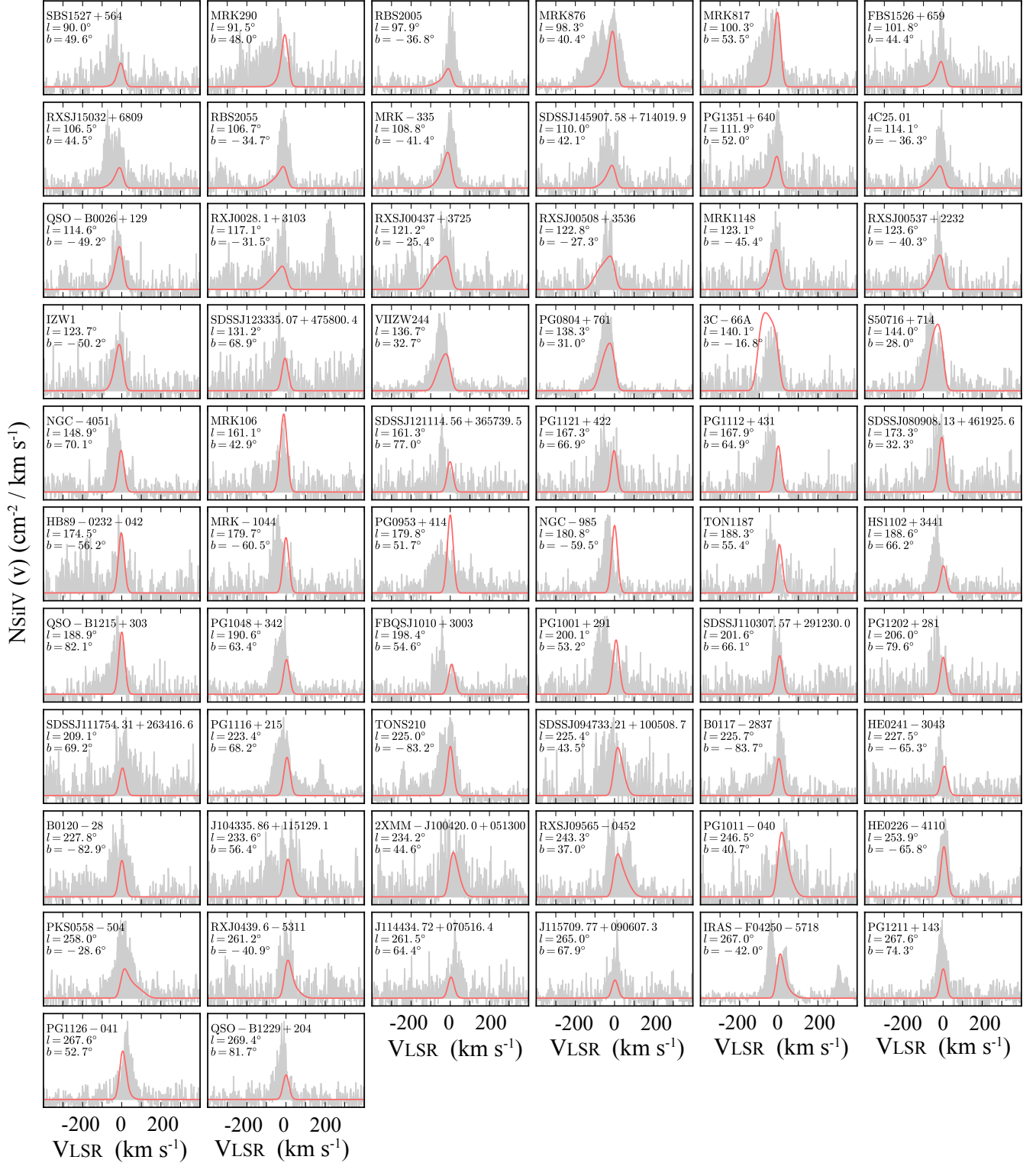


**Figure 3.** Shown in red are the modeled Si IV column density profiles predicted by the *rotation-only* model of the MW's D/H interface (§ 3.2.2). In gray shade we show the observed profiles seen towards background QSO sightlines as derived in § 3.1, which include the Si IV not only from the MW's D/H interface but also from other components along the QSO paths (see § 4). The QSO sightlines here are all towards the outer Galaxy directions with  $90^\circ < l < 270^\circ$ . For clarity, we do not show the column density scale in this figure. Please see Fig 6 for the examples of column density scale.

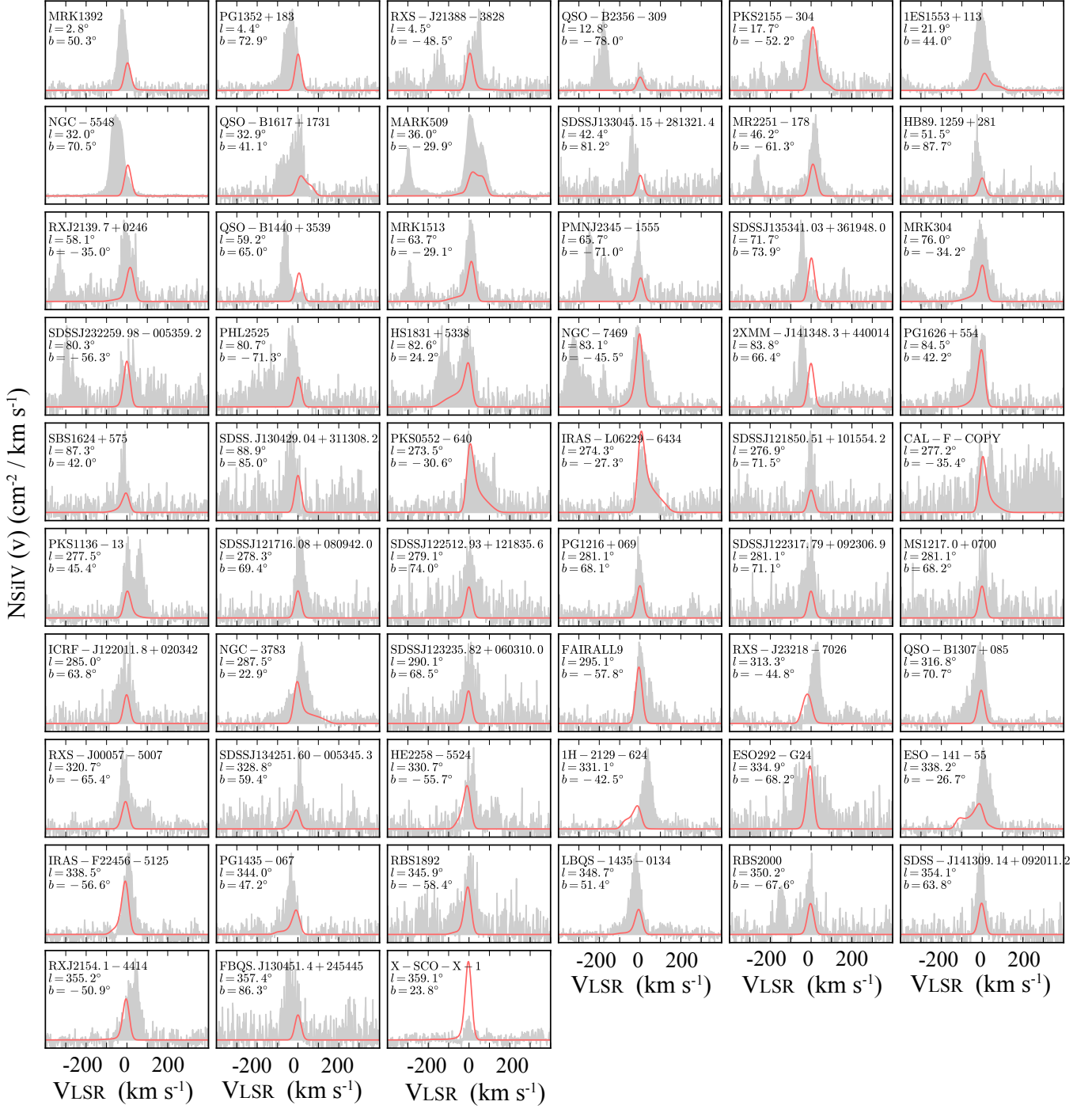


**Figure 4.** Refer to Fig 3. The QSO sightlines shown here all lie in the direction of the inner Galaxy with  $0^\circ < l < 90^\circ$  or  $270^\circ < l < 360^\circ$ .

flat-slab parameters ( $n_0$ ,  $z_h$ ) and the direction of the sightline. This is to say, our 3D kinematic model produces the same amount Si IV as SW09's 1D flat slab along any given line of sight (see Fig 5).

We use the *rotation-only* model to predict the Si IV column density profiles of the MW's D/H interface along the 119 QSO sightlines, and compare them with the ob-

served profiles we derive in § 3.1. We show the comparison in Fig 3 for QSO sightlines towards the outer Galaxy ( $90^\circ < l < 270^\circ$ ) and in Fig 4 for those towards the inner Galaxy ( $0^\circ < l < 90^\circ$  or  $270^\circ < l < 360^\circ$ ). The modeled profiles show that most of the Si IV at the MW's D/H interface moves at  $|v| < 100 \text{ km s}^{-1}$  with only a few sightlines exhibiting a weak tail towards high veloc-

ities. Since QSO paths go through not only the MW’s D/H interface but also other components such as the CGM, the observed profiles will include more Si IV than the modeled ones. Along most of the sightlines shown in Fig 3 and 4, we find additional Si IV in excess of the predicted D/H profiles. Our findings of Si IV excess that does not belong to the MW’s D/H interface agrees with that of SW09, who also reported ion column density excesses seen towards background QSOs. We will examine the significance of this Si IV excess in § 3.3.

In a few cases, our 3D model generates profiles that over-predict the observed ones, such as X-SCO-X-1 (in Fig 4) and 3C-66A (in Fig 3). There are two primary reasons for this over-prediction. First, towards some sightlines, the ionized gas may be so hot that Si IV is not the dominant ionization state. For example, we find that X-SCO-X-1 is at  $l = 359.1^\circ$ ,  $b = 23.8^\circ$ , in the direction of the northern Fermi Bubble (Fox et al. 2015; Bordoloi et al. 2017). Second, the patchiness of the MW’s D/H interface and the CGM may result in some Si IV holes along the line of sight that leads to modest over-prediction, such as those along 3C-66A, PG0953+414, NGC-985, and 2XMM-J141348.3+440014.

In Fig 5, we reproduce the  $N_{\text{SiIV}} \sin|b| - \log|z|$  relation as studied in SW09. Blue circles and squares show the observed  $N_{\text{SiIV}}$  along the stellar and QSO sightlines from SW09, and red triangles indicate the observed  $N_{\text{SiIV}}$  integrated from  $-100$  to  $100 \text{ km s}^{-1}$  towards the 119 QSOs we used in this work. For all the data points in SW09’s and our sample, we use the *rotation-only* model to predict the Si IV column density profile and calculate the total Si IV column density at  $|v| < 100 \text{ km s}^{-1}$ . The model-predicted  $N_{\text{SiIV}}$  are shown as black dots, which exhibits the same  $N_{\text{SiIV}} \sin|b| - \log|z|$  relation as predicted by SW09’s 1D flat slab. Fig 5 demonstrates that our 3D flat slab, the *rotation-only* model, has covered most of the Si IV at the MW’s D/H interface. There is a significant Si IV excess seen towards background QSOs that does not belong to the MW’s D/H interface (see the red triangles and blue squares).

### 3.2.3. Gas Inflows, Halo Lagging, and Turbulence Broadening

In § 3.2.2, we use the *rotation-only* model to predict the Si IV column density profiles of the MW’s D/H interface and find most of the modeled Si IV moves at  $|v| < 100 \text{ km s}^{-1}$ . We now incorporate gas inflows  $v_{\text{in}}$ , halo lagging  $v_{\text{lag}}$ , and turbulent broadening  $b_{\text{turb}}$  into the model, and examine whether these additional kinematic parameters change the velocity distribution of the Si IV at the D/H interface along a given line of sight. In particular, we aim to investigate whether the modeled Si IV would move at higher velocities than  $|v| > 100 \text{ km s}^{-1}$  under various kinematic conditions. We select

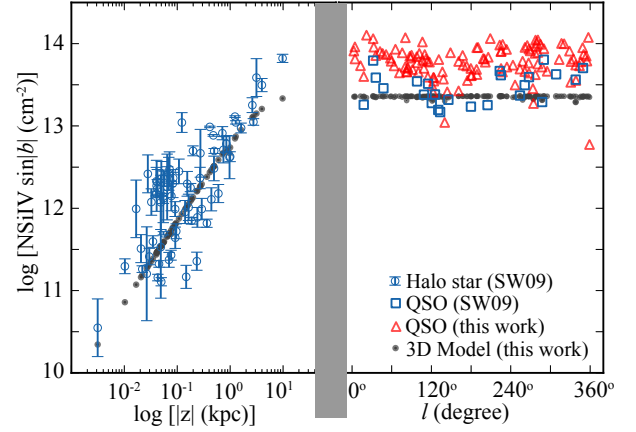


**Figure 5.** The  $\log(N_{\text{SiIV}} \sin|b|) - \log|z|$  relation on the left for stellar sightlines, and  $\log(N_{\text{SiIV}} \sin|b|) - l$  on the right for QSO sightlines, where  $z$  is the distance of a given star from the Galactic plane and  $b/l$  is the Galactic latitude/longitude. The blue symbols are measurements from SW09: the open circles are for nearby halo stars, and the squares are for QSO sightlines. We do not use those data with upper or lower column density limits. The red triangles are from our QSO measurements, with column densities integrated from  $-100$  to  $100 \text{ km s}^{-1}$ . Error bars on the QSO sightlines are approximately equal to the size of the symbol. The black dots show the corresponding modeled column densities expected in our 3D flat slab, the *rotation-only* model. For each stellar sightline, the modeled path ends at the position of the star; for each QSO sightline, the modeled path ends at 300 kpc. This plot is similar to the Si IV panel of Fig 2 in SW09, showing that our 3D kinematic model is consistent with SW09’s 1D model regarding the total Si IV content along the stellar lines of sight. The underprediction of Si IV towards QSO sightlines in the right part of the figure suggests that there is a significant amount of Si IV beyond the MW’s D/H interface.

three typical QSOs at low/medium/high Galactic latitudes to illustrate how varying these parameters affects the Si IV column density profiles in different directions in Fig 6. We note that our implementation of different kinematics changes only the velocity distribution of Si IV along a given line of sight, but not the total Si IV column density.

In the left column of Fig 6, we adopt inflow velocities of  $v_{\text{in}} = 0$  (solid),  $-30$  (dashed), and  $-60$  (dotted)  $\text{km s}^{-1}$ . This range reflects the observed intermediate-velocity sky of the MW, which has been found to be predominantly infalling (van Woerden et al. 2004; Putman et al. 2012). In each of the three panels 1a/2a/3a, we show that the velocity peak gradually shifts leftward as we increase the inflow velocity. Comparing  $N_{\text{SiIV}}(v)$  profiles at different Galactic latitudes in the three panels, we find higher Galactic latitude yields a greater shift to more negative velocities. Since the inflow is implemented such that gas accretes perpendicularly towards the Galactic disk, sightlines with higher  $b$  will have larger projected inflow velocity than those with



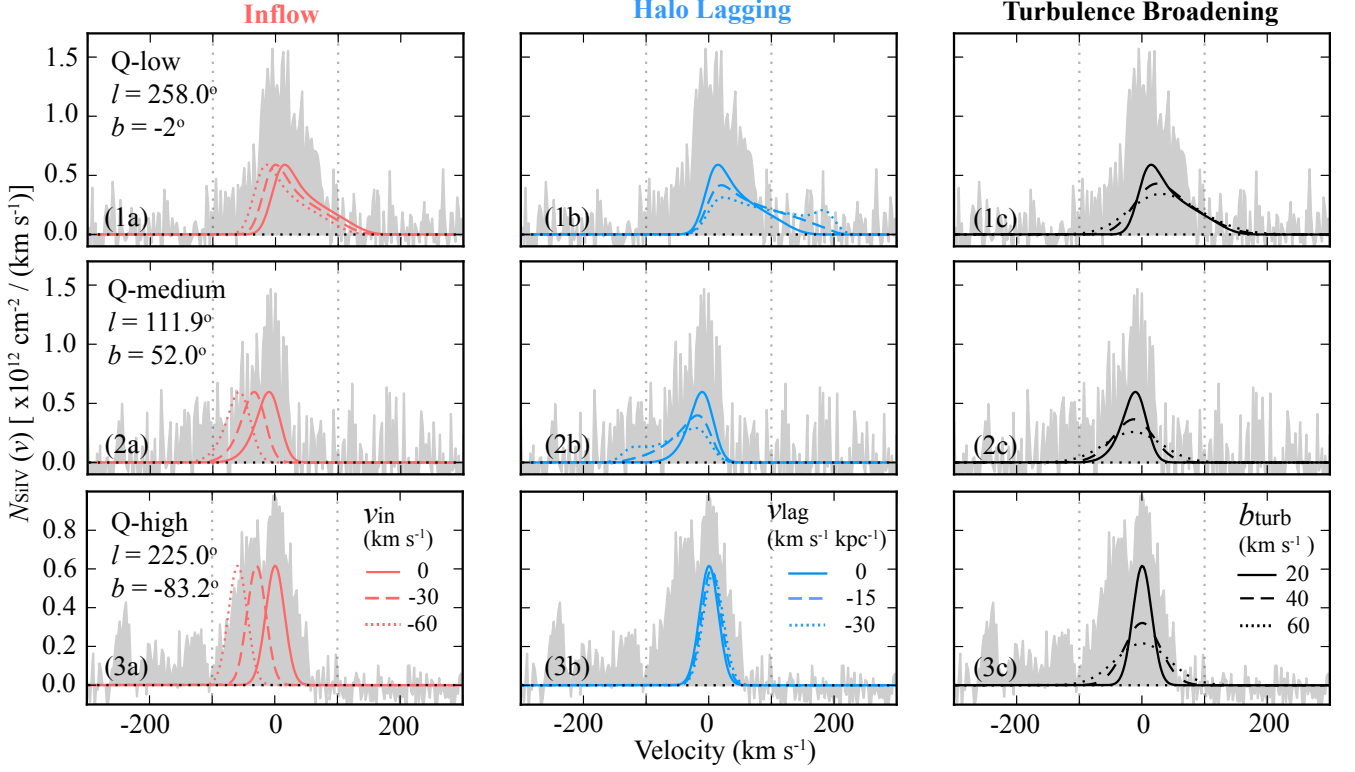


**Figure 6.** The modeled Si IV column density profiles  $N_{\text{SiIV}}(v)$  with different kinematic parameter inputs. We select three QSOs at low/medium/high Galactic latitudes to show how inflows ( $v_{\text{in}} = 0, -30, -60 \text{ km s}^{-1}$ ; left column), halo lagging ( $v_{\text{lag}} = 0, -15, -30 \text{ km s}^{-1} \text{ kpc}^{-1}$ ; middle column), and turbulent broadening ( $b_{\text{turb}} = 20, 40, 60 \text{ km s}^{-1}$ ; right column) affect the modeled profiles in different directions. The three QSOs are PKS0558-504 (Q-low), PG1351+640 (Q-medium), and TONS210 (Q-high). The solid curve and gray shaded area in each panel are the same as in Fig 3 and 4.

lower  $b$ .

In the middle column, we examine the effect of halo lagging, which is the deceleration of rotation velocity as one moves away from the Galactic plane. We modify the halo lagging term as  $v_{\text{lag}} = 0$  (solid),  $-15$  (dashed),  $-30$  (dotted)  $\text{km s}^{-1} \text{ kpc}^{-1}$ . We base this range on observations of halo lagging measured in nearby edge-on galaxies (e.g., [Fraternali & Binney 2006](#)) as well as our own MW's D/H interface ( $v_{\text{lag}} = -22 \pm 6 \text{ km s}^{-1} \text{ kpc}^{-1}$ ; [Levine et al. 2008](#)). At high Galactic latitude towards the Galactic poles, halo lagging has little effect on the column density profiles because the projection of D/H rotation is close to  $0 \text{ km s}^{-1}$ . This effect is shown in panel 3b, where the modeled curves with different  $v_{\text{lag}}$  overlap almost entirely. For sightlines at lower  $b$ , the  $N_{\text{SiIV}}(v)$  profiles vary considerably from sightline to sightline, depending on both  $l$  and  $b$ . Towards  $l \sim 90^\circ$  (panel 2b), the flat slab appears at negative velocities in the LSR frame, which produces a degeneracy with gas inflows. On the other hand, towards  $l \sim 270^\circ$  (panel 1b) the flat slab is seen at positive velocities in the LSR frame, an effect which may be confused with outflows.

Finally, in the right-hand column, we vary the turbulent broadening as  $b_{\text{turb}} = 20$  (solid),  $40$  (dashed),  $60$

(dotted)  $\text{km s}^{-1}$ . While the line profiles broaden with increasing  $b_{\text{turb}}$ , the velocity peaks remain unchanged.

In summary, Fig 6 shows that varying kinematic parameters such as inflow velocity  $v_{\text{in}}$ , halo lagging  $v_{\text{lag}}$ , and turbulent broadening  $b_{\text{turb}}$ , may have a considerable effect on Si IV apparent column density profiles as a function of both Galactic latitude  $l$  and Galactic longitude  $b$ ; however, most of the modeled Si IV at the D/H interface remains at  $|v| < 100 \text{ km s}^{-1}$ . In the remainder of this manuscript, we focus on the *rotation-only* model to examine the Si IV excess at  $|v| < 100 \text{ km s}^{-1}$  beyond the MW's D/H interface and note that other kinematic behaviors do not change our results significantly.

### 3.3. The Significance of the Si IV Excess

A key finding of our analyses in § 3.2 is that the Si IV column density seen towards background QSOs lies in excess of the simple D/H model predictions and most of the excess is found at  $|v| < 100 \text{ km s}^{-1}$  regardless of various kinematic implementations. To quantify the significance of the Si IV excess, we compute the fraction of the Si IV excess with respect to the total amount of Si IV seen along the QSO sightlines at  $|v| < 100 \text{ km s}^{-1}$ , expressed as  $f_1 = N_{\text{ex}, |v| < 100} / N_{\text{obs}, |v| < 100}$ . In the

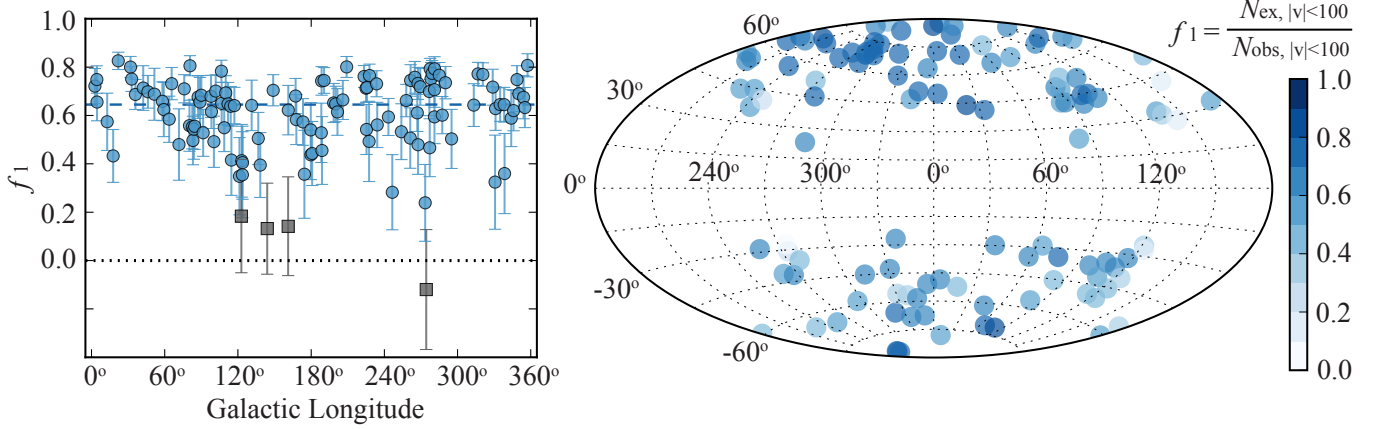


**Figure 7.** The fraction of the Si IV excess with respect to the total Si IV column density seen towards background QSOs integrated over the range of  $|v| < 100 \text{ km s}^{-1}$ , expressed as  $f_1 = N_{\text{ex}, |v| < 100} / N_{\text{obs}, |v| < 100}$  (see § 3.3). In the left panel, gray squares are for those sightlines with Si IV mostly from the MW’s D/H interface. Blue dots are for the remaining QSO sightlines, which show a large fraction of Si IV excess that does not belong to the D/H interface. The blue line shows the median of the Si IV excess fraction at  $f_{\text{ex}, |v| < 100} = 0.64$ .

equation  $N_{\text{ex}, |v| < 100} \equiv \int_{-100}^{100} (N_{\text{obs}}(v) - N_{\text{mod}}(v)) dv$  and  $N_{\text{obs}, |v| < 100} \equiv \int_{-100}^{100} N_{\text{obs}}(v) dv$ , where  $N_{\text{obs}}(v)$  is the observed Si IV column density profile and  $N_{\text{mod}}(v)$  is the modeled profile from the *rotation-only* model.

We show the distribution of  $f_1$  in Fig 7. Four sightlines<sup>5</sup> (in gray squares) have  $f_1 \sim 0$  within the errors, indicating that the model predicts a similar amount of Si IV as the observed values or there is no excess beyond the D/H interface along these sightlines. For the remaining sightlines, shown as blue dots, we find the Si IV excess accounts for  $\sim 25\%$ - $80\%$  of the total observed Si IV column densities. The median and mean values of  $f_1$  are 0.64 and  $0.62 \pm 0.13$ , respectively, where 0.13 is the standard deviation. We show the sky distribution of  $f_1$  in the right panel. In general,  $f_1$  is not sensitive to  $l$  and  $b$ , indicating that the Si IV excess is likely to be a global phenomenon in the MW. There might be a slight enhancement of  $f_1$  towards the Galactic center and the north Galactic pole, consistent with the findings of column density enhancement near these regions in SW09 and Wakker et al. (2012). Fig 7 shows the Si IV from the MW’s D/H interface only accounts for 36% of the total Si IV column densities seen towards background QSOs at  $|v| < 100 \text{ km s}^{-1}$ , with the remaining 64% contributed by material that does not belong to the D/H interface.

Along many sightlines we find high-velocity peaks at  $|v| > 100 \text{ km s}^{-1}$  (see Fig 3 & 4), which likely arise from the ionized high-velocity clouds floating in the MW’s CGM (e.g., Fox et al. 2006, Shull et al. 2009)

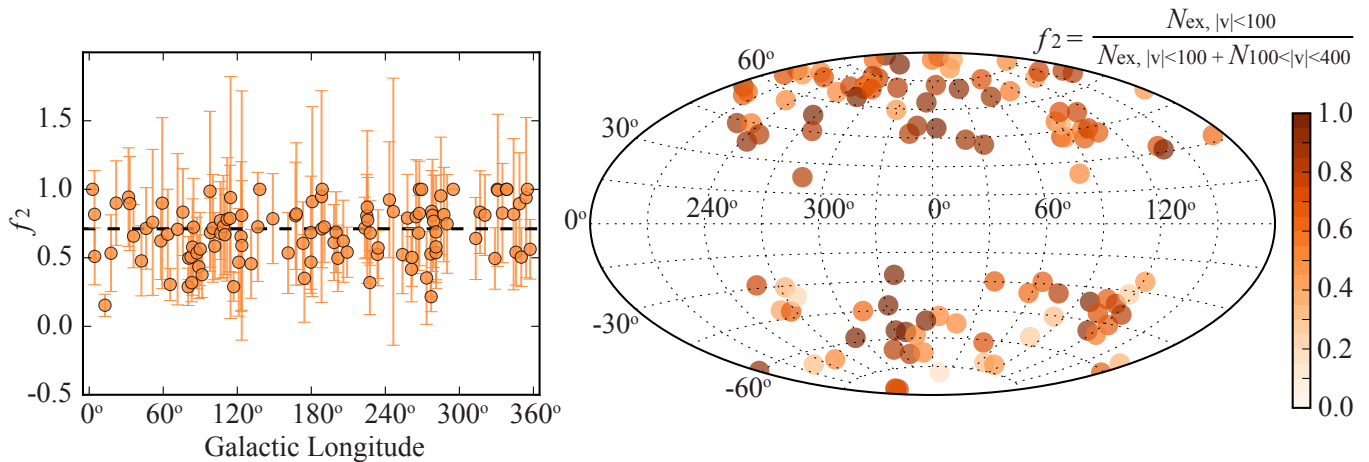
or from material associated with the ionized extension of the Magellanic System (Fox et al. 2014). This is not considered as the excess since the MW’s D/H models do not show dominant Si IV moving at  $|v| > 100 \text{ km s}^{-1}$ . We now compare the Si IV excess to the high-velocity gas at  $100 < |v| < 400 \text{ km s}^{-1}$ . We calculate the ratio of the Si IV excess to the total amount of Si IV that does not belong to the MW’s D/H interface including the high-velocity peaks, expressed as  $f_2 = N_{\text{ex}, |v| < 100} / (N_{\text{ex}, |v| < 100} + N_{100 < |v| < 400})$ , where  $N_{100 < |v| < 400}$  is the total column density of the high-velocity gas integrated over  $100 < |v| < 400 \text{ km s}^{-1}$ .

Fig 8 shows the distribution of  $f_2$ . A value of  $f_2 \geq 1.0$  indicates an absence of high-velocity peaks and the larger-than-unity value is due to noise. For these sightlines, we manually set  $f_2$  to 1.0 and the corresponding error to 0.0. The left panel shows that the Si IV excess accounts for a significant fraction of the material that is not associated with the MW’s D/H interface. The horizontal line indicates the median value of  $f_2$  at 0.71; the mean value is  $0.69 \pm 0.20$  where 0.20 is the standard deviation. The sky distribution in the right panel shows that  $f_2$  does not vary significantly across the Galactic sky. Fig 8 shows that the Si IV excess accounts for 71% of the total material that does not belong to the MW’s D/H interface. A comparison of the Si IV excess and the high-velocity gas finds a mass ratio of  $71\%:29\% \approx 2.4:1$ . We will further discuss the implication of this mass ratio in § 4.2.

#### 4. DISCUSSION

We have modeled the MW’s D/H interface as a 3D flat slab and shown that there is clear Si IV excess unaccounted for in the D/H model at  $|v| < 100 \text{ km s}^{-1}$ . Here

<sup>5</sup> IRAS-L06229-6434, RXSJ00508+3536, S50716+714, and MRK106



**Figure 8.** The ratio of the Si IV excess to the total amount of Si IV beyond the MW’s D/H interface including the high-velocity gas, expressed as  $f_2 = N_{\text{ex}, |v| < 100} / (N_{\text{ex}, |v| < 100} + N_{100 < |v| < 400})$  (see § 3.3), where  $N_{100 < |v| < 400}$  is the total column density of high-velocity gas integrated over the range of  $100 < |v| < 400 \text{ km s}^{-1}$ , and  $N_{\text{ex}, |v| < 100}$  is the same as in Fig 7. The value  $f_2$  enables us to quantify the fraction of gas moving at  $|v| < 100 \text{ km s}^{-1}$  hidden behind the MW’s D/H interface that is often neglected in high-velocity-focused studies.

we proceed to discuss different sources that might contribute to the Si IV excess and present evidence for the unlikely and likely origin scenarios in § 4.1.1 and 4.1.2, respectively. Adopting the CGM origin in 4.2, we conduct an order-of-magnitude calculation of the gas mass of the MW’s CGM moving at  $|v| \leq 100 \text{ km s}^{-1}$  and compare this to previous CGM halo mass values.

#### 4.1. Origins of the Si IV Excess

##### 4.1.1. Unlikely Scenarios

In this section, we consider several ionized structures that the QSO paths may intercept, including the Local Bubble, Intermediate-Velocity Clouds, and the Local Group. As we reason below, we find these scenarios are unlikely to be dominant contributors to the Si IV excess.

First, it is unlikely our sightlines would intercept dense spiral-arm regions or warps at the outskirts of the disk since the QSOs are mostly at  $|b| \gtrsim 20^\circ$ . On the other hand, all sightlines must leave the disk through the Local Bubble (LB), which is a cavity in the MW’s ISM that surrounds us with a radius of  $\sim 100 \text{ pc}$ . Savage & Lehner (2006) found the O VI column density from the LB only contributes  $\sim 9\%$  of the total column along sightlines towards MW’s halo stars through comparison with UV spectra of nearby white dwarfs at a mean distance of  $\sim 109 \text{ pc}$ . Based on this, SW09 concluded that the ions from the LB would not significantly affect the calculations of  $(z_h, n_0)$  of the flat slab’s exponential profile. Since our 3D kinematic model adopts their best-fit values  $(z_h, n_0)$ , we suffer the same degree of contamination and the LB effect is negligible.

Second, intermediate-velocity clouds (IVCs) are defined as discrete H I clouds moving at velocities  $|v| < 100$

$\text{km s}^{-1}$  (van Woerden et al. 2004; Albert & Danly 2004; Wakker 2004). Distance measurements of IVCs using halo stars find a  $|z|$  height of  $\sim 1\text{--}5 \text{ kpc}$  (see Table 2 in Albert & Danly 2004). Given the SW09’s D/H flat-slab model has a scale height of  $3.2 \text{ kpc}$  for the Si IV, it already includes most of what would be the ionized counterpart of the IVCs.

Lastly, we consider whether ionized gas beyond the MW, especially in the Local Group, may contribute to the Si IV excess since the QSOs lie at higher redshifts. We make two arguments that this scenario is unlikely. First, ion column densities (e.g., Si II, Si III) drop significantly beyond  $160 \text{ kpc}$  ( $\sim 0.5 R_{\text{vir}}$ ) in several extragalactic surveys (Werk et al. 2013, 2014; Liang & Chen 2014), so it would be unusual for a significant column density of metals to be found beyond this radius in the intergalactic medium. Second, the Si IV excess shows no evidence for a preference along the Local Group axis, indicating that there is no significant contribution from the ionized gas in the Local Group. Therefore, ionized gas beyond the MW’s CGM is unlikely to contribute significantly to the Si IV excess seen towards QSO sightlines across the Galactic sky.

##### 4.1.2. The Likely Scenario: The Galactic CGM

The MW’s CGM is the most likely origin of the Si IV excess given its nearly uniform distribution across the Galactic sky toward background QSOs. The origin of the CGM absorption could be: (1) a low-velocity counterpart of the ionized high-velocity clouds (HVCs), (2) gas associated with the Fermi Bubbles, and/or (3) gas in a large volume of the MW’s CGM similar to that observed for other low- $z$   $L^*$  galaxies. In this section, we discuss these scenarios separately.

HVCs are defined in H I 21-cm observations as the neutral hydrogen moving at  $|v| \gtrsim 100 \text{ km s}^{-1}$  (van Woerden et al. 2004; Putman et al. 2012). Since we are discussing the origin of the Si IV column density excess at  $|v| < 100 \text{ km s}^{-1}$ , HVCs themselves are not the possible culprits; however, clouds have been found with similar properties to HVCs moving at lower velocities (Peek et al. 2009; Saul et al. 2014), as expected from models (Wakker 1991). HVCs tend to be less metal-rich and are found at larger distances from the Galactic plane than the IVCs. An often-quoted HVC distance is  $\sim 10 \text{ kpc}$  (e.g., see Table 1 in Wakker 2004). The ionized components of the H I HVCs have been detected in multiple phases, including Si IV (e.g., Fox et al. 2005, Fox et al. 2006, Shull et al. 2009). The Si IV excess we find is likely to be at least partially due to clouds moving at  $|v| < 100 \text{ km s}^{-1}$  akin to the ionized HVCs. We further discuss in § 4.2.1 what the mass of the Si IV excess would be if it were related to the low-velocity counterpart of the ionized HVCs.

The Fermi Bubbles are large bi-conical lobes detected in  $\gamma$ -rays extending  $\pm 55^\circ$  above/below the Galactic center (Dobler et al. 2010; Fox et al. 2015; Bordoloi et al. 2017). Since the Fermi Bubbles only occupy a small region of the Galactic sky, it would not be the major source of the excess seen towards most of our QSO sightlines. Towards the Galactic center it is possible that a fraction of the Si IV excess comes from the projected low-velocity components of the Fermi Bubbles.

Given the Si IV excess is seen towards most of our sightlines, it is most likely to be a global phenomenon associated with the more extended volume of the MW's CGM. In general, the MW's CGM is only studied at high velocities ( $|v| > 100 \text{ km s}^{-1}$ ) to avoid the contamination of the nearby low-velocity gas. However, Z15 found that  $\sim 65\%$  of the MW's CGM mass above  $|b| \geq 20^\circ$  is likely to be hidden at  $|v| \leq 100 \text{ km s}^{-1}$  regardless of the gas phase, based on synthetic observations of a simulated MW-mass galaxy from a cosmological simulation (Joung et al. 2012). If the Si IV excess is the low-velocity component of the Si IV absorption due to the CGM, from § 3.3 we find  $\sim 71\%$  of the Si IV-probed CGM is at velocities  $|v| \leq 100 \text{ km s}^{-1}$ . This is therefore consistent with the hidden CGM fraction estimated in Z15. We further discuss this scenario in § 4.2.2.

#### 4.2. Order-of-Magnitude Calculations for the MW's Hidden CGM Mass

As discussed in the previous section, the most likely scenario is the Si IV excess resides in the MW's CGM, and it accounts for 71% of the total CGM Si IV mass. The existence of a dominant low-velocity component is consistent with the CGM studies of other galaxies. Extragalactic studies find the centroid velocities of the ions

detected in the CGM are mostly within  $\pm 100 \text{ km s}^{-1}$  from the hosts' systemic velocities, regardless of the impact parameters of the ion detections (e.g., Werk et al. 2013).

In this section, we conduct order-of-magnitude calculations of the Si IV mass in the MW's CGM as revealed by the Si IV excess. We assume the MW's CGM gas probed by other ions (e.g., Si II, C IV) is similarly hidden at  $|v| < 100 \text{ km s}^{-1}$  as the Si IV-bearing gas, as predicted in the simulation work of Z15. With this assumption, we convert the calculated Si IV mass to a total hydrogen mass and use the 71% hidden fraction to infer the total CGM mass.

##### 4.2.1. Low-Velocity Gas Associated With the Ionized HVCs

We first consider the case that the Si IV excess is partially associated with the low-velocity counterpart of the ionized HVCs (e.g., Fox et al. 2006; Shull et al. 2009; Lehner & Howk 2011). We consider a geometry with a second cylindrical flat slab above the MW's D/H interface. As long as the slab is close enough to the disk that all of our sightlines cross it, our mass estimate is only a function of the measured Si IV column density excess and an assumed area. We find the total hidden mass of Si IV associated with this second flat slab is  $M_{\text{SiIV}} = \pi R^2 m_{\text{SiIV}} N_{\text{ex},|v|<100} \times 2 \approx 5.9 \times 10^4 M_\odot \left(\frac{R}{28 \text{ kpc}}\right)^2$ , where  $N_{\text{ex},|v|<100} = 5.3 \times 10^{13} \text{ cm}^{-2}$  is the mean Si IV excess column density measured towards the QSO sightlines,  $m_{\text{SiIV}}$  is the mass of the silicon atom, and the factor 2 accounts for the gas on both sides of the disk.  $R$  is the radius of the second flat-slab cylinder, adopted as 28 kpc according to the study of the MW's disk extension and vertical structure in Levine et al. (2006).

We convert the Si IV mass into a hydrogen mass as  $M_{\text{hidden}} = \left(\frac{M_{\text{SiIV}}}{m_{\text{SiIV}}}\right) 1.4 m_{\text{H}} f_{\text{SiIV}}^{-1} (\text{Si/H})_\odot^{-1} Z^{-1}$ , where 1.4 is to account for the presence of helium and  $m_{\text{H}}$  is the mass of the hydrogen atom. The subscript *hidden* suggests that this low-velocity component is hidden behind the foreground medium thus has been commonly neglected. We adopt  $(\text{Si/H})_\odot = 10^{-4.49}$  from Asplund et al. (2009), which is the silicon abundance in the present-day solar photosphere relative to hydrogen. We assume the metallicity as  $Z = 0.2 Z_\odot$ , a value adopted by Lehner & Howk (2011) to estimate the mass of the ionized HVCs in the MW based on Complex C measurements (Wakker et al. 2001). The most uncertain term is the ionization fraction  $f_{\text{SiIV}}$ , defined as the ratio of the Si IV to all the silicon in various neutral and ionized states. Photoionization, collisional ionization, and other non-equilibrium processes such as shock ionization, conductive interfaces, and turbulence mixing may contribute to producing Si IV (e.g., Fox et al. 2005, Wakker et al. 2012). As we aim for an order-of-magnitude mass calculation, we do not conduct sophisticated ionization mod-



eling to determine  $f_{\text{SiIV}}$ . Based on the collisional ionization model of (Gnat & Sternberg 2007), we adopt  $f_{\text{SiIV}} = 0.4$  which is the maximum ionization fraction of Si IV for  $Z = 0.1 Z_{\odot}$ . We also examine the Si IV ionization fraction produced by CLOUDY (v13.03; Ferland et al. 1998, 2013) in an extragalactic UV background (Haardt & Madau 2001) at H I column density of  $10^{20} \text{ cm}^{-2}$ , and found the maximum  $f_{\text{SiIV}} \sim 0.3$  at  $Z = 0.1 - 0.3 Z_{\odot}$ , similar to the collisional ionization prediction. We find the total hidden mass at  $|v| < 100 \text{ km s}^{-1}$  is  $M_{\text{hidden}} \sim 1.1 \times 10^9 M_{\odot} (\frac{R_{\text{HVC}}}{28 \text{ kpc}})^2 (\frac{f_{\text{SiIV}}}{0.4})^{-1} (\frac{Z}{0.2 Z_{\odot}})^{-1}$ . Considering the mass ratio of the Si IV excess to high-velocity gas of 2.4:1 as derived in 3.3, we find that the ionized high-velocity gas in the MW should have a mass of  $\sim 5 \times 10^8 M_{\odot}$ .

We compare our estimate with the mass of the ionized HVCs studied in Lehner & Howk (2011). Lehner & Howk searched for ionized HVC signatures towards 28 halo star sightlines and found a detection rate of  $f_c = 0.5$ . Assuming a distance of 12 kpc and taking into account the detection rate, they found  $M_{\text{HVCs}} = 1.1 \times 10^8 M_{\odot} (\frac{d}{12 \text{ kpc}})^2 (\frac{f_c}{0.5}) (\frac{Z}{0.2 Z_{\odot}})^{-1}$ . In the calculation, they assumed a spherical geometry with an area of  $4\pi d^2$  for the ionized HVCs. Since the assumed sphere only extends 12 kpc from the Sun, we caution their mass estimate may not cover the whole ionized HVC population over the Galactic plane.

We recalculate the total mass for the observed ionized HVC population using the H II column density  $N_{\text{HII}} \approx 1.1 \times 10^{19} \text{ cm}^{-2} (\frac{Z}{0.2 Z_{\odot}})^{-1}$  provided in Lehner & Howk (2011). Assuming the same cylindrical flat slab as we adopt in the previous calculation, we find a mass of  $\sim 6 \times 10^8 M_{\odot} (\frac{R}{28 \text{ kpc}})^2 (\frac{N_{\text{HII}}}{1.1 \times 10^{19} \text{ cm}^{-2}}) (\frac{Z}{0.2 Z_{\odot}})^{-1}$ , consistent with our previous high-velocity mass estimate based on the mass ratio of Si IV excess to high-velocity gas. Note that in our mass calculations we do not consider the HVC detection rate  $f_c = 50\%$  as provided in Lehner & Howk (2011). The consistency suggests that current observations of the ionized HVCs are likely to have missed the low-velocity counterpart in the inner Galactic halo moving at  $|v| < 100 \text{ km s}^{-1}$ .

#### 4.2.2. A Larger Volume in the MW's CGM

As found in extragalactic CGM studies, highly ionized gas can extend to nearly half the virial radii of the host galaxies (e.g., Werk et al. 2014; Liang & Chen 2014). Therefore, it is more likely that the Si IV in the MW's CGM also has such large extension instead of merely concentrating in the inner Galactic halo. Here we assume the Si IV excess to be due to the MW's CGM with a radius of  $R_{\text{CGM}} = 160 \text{ kpc}$ . This is the radius probed by the COS-Halos survey (Tumlinson et al. 2011; Werk et al. 2014; Prochaska et al. 2017). The total Si IV mass is  $M_{\text{SiIV}} = \frac{4}{3} \pi R_{\text{CGM}}^3 \rho_{\text{SiIV}} = \frac{4}{3} \pi R_{\text{CGM}}^2 m_{\text{SiIV}} N_{\text{ex},|v|<100}$ ,

where  $\rho_{\text{SiIV}} = m_{\text{SiIV}} N_{\text{ex},|v|<100} / R_{\text{CGM}}$  is the Si IV mean density in the Galactic halo. We find that the MW's hidden CGM has a total Si IV mass of  $M_{\text{SiIV}} \sim 1.3 \times 10^6 M_{\odot} (\frac{R_{\text{CGM}}}{160 \text{ kpc}})^2$ . We apply a similar calculation to that laid out in § 4.2.1 in order to convert the Si IV mass to a hydrogen mass:  $M_{\text{hidden}} \sim 1.6 \times 10^{10} M_{\odot} (\frac{R_{\text{CGM}}}{160 \text{ kpc}})^2 (\frac{f_{\text{SiIV}}}{0.4})^{-1} (\frac{Z}{0.3 Z_{\odot}})^{-1}$ . Again, we adopt an ionization fraction  $f_{\text{SiIV}}$  of 0.40 based on Gnat & Sternberg (2007) and a metallicity,  $Z$ , based on the COS-Halos mean CGM metallicity of  $Z = 0.3 Z_{\odot}$  (Prochaska et al. 2017). Considering the mass ratio of Si IV excess to the high-velocity gas of 2.4:1 (see §3.3), we find that the total mass of the MW's CGM, including the high-velocity gas, is  $\sim 2.3 \times 10^{10} M_{\odot}$ .

Our derived mass is at the lower end of the most recent CGM mass estimates from the COS-Halos team (Prochaska et al. 2017), who found the total mass of the cool, photoionized CGM of  $L \sim L^*$  galaxies at  $z \sim 0.2$  is  $9.2 \pm 4.3 \times 10^{10} M_{\odot} (\frac{R_{\text{CGM}}}{160 \text{ kpc}})^2$ . It is more consistent with the CGM mass estimate ( $\log(M/M_{\odot}) = 10.5 \pm 0.3$ ) provided by Keeney et al. (2017). The discrepancy between the COS-Halos' result and that of Keeney et al. (2017) is mainly due to the different treatment of the extragalactic UV ionization background. Our calculation indicates that the MW is likely to host a similarly massive CGM as those  $L^*$  galaxies at low- $z$ .

We caution that the Si IV ionization fraction is highly uncertain without fully understanding its ionization mechanism (e.g. Werk et al. 2016). Additionally, metallicity measurements for the ionized gas are notoriously difficult to obtain. For this reason, our value for the MW's ionized CGM mass is accurate only as an order-of-magnitude estimate. Large systematic uncertainties in gas ionization state and  $Z$  plague all mass estimates based upon ionized gas absorption lines.

## 5. CONCLUSION

For MW absorption-line studies that rely on background QSOs, the lines of sight unavoidably intercept the ISM, the D/H interface, and the CGM of the MW. Therefore every QSO spectrum contains mixed absorption-line components from these MW sources. Traditionally, high-velocity gas ( $|v| \gtrsim 100 \text{ km s}^{-1}$ ) is assumed to be associated with the CGM, while gas at  $|v| \lesssim 100 \text{ km s}^{-1}$  is considered to be more nearby. In this work, we examine the significance of the ionized gas moving at  $|v| < 100 \text{ km s}^{-1}$  in the MW's CGM that is commonly neglected in high-velocity-focused studies.

We carefully select a sample of HST/COS spectra of 119 QSO at  $|b| > 20^\circ$  from the HSLA and analyze the Si IV doublets to obtain the Si IV column density profiles towards different directions of the Galactic sky. To separate the signals of the CGM and nearby gas in the profiles, we adopt SW09's 1D flat-slab model of the MW's

D/H interface and transform it into a 3D kinematic flat-slab model. We incorporate co-rotation, halo lagging, gas inflow, and turbulence broadening in the model. Our 3D model preserves the total Si IV column density quantity as yielded from SW09’s 1D flat slab, and predicts the Si IV column density profiles along any given line of sight. We compare the modeled Si IV profiles of the MW’s D/H interface with those observed towards the 119 QSO sightlines. We find the Si IV content at the MW’s D/H interface only accounts for 36% of the observed Si IV column density towards these QSO sightlines from  $-100$  to  $100 \text{ km s}^{-1}$  (see Fig 7). We refer to the remaining 64% that is unaccounted for as the Si IV excess. When one examines the Si IV excess in the context of all the Si IV moving at  $|v| < 400 \text{ km s}^{-1}$  unassociated with the MW’s D/H interface, we find that the Si IV excess contributes 71% of the mass (see Fig 8).

We find that the origin of the Si IV excess is unlikely to be the Local Bubble, the MW’s IVCs, or the Local Group. Since the Si IV excess is seen in the vast majority of our sightlines across the Galactic sky, we conclude that the excess most likely resides in the MW’s CGM. This indicates that current observations of the high-velocity gas in the MW’s CGM are missing a significant fraction (71%) of the CGM mass hidden at  $|v| < 100 \text{ km s}^{-1}$ . This hidden CGM fraction is consistent with the value predicted by Z15 who, using a MW simulation, found that  $\sim 65\%$  of the MW’s CGM is likely to move at  $|v| < 100 \text{ km s}^{-1}$ .

We conduct an order-of-magnitude calculation for the MW’s CGM mass taking into account the hidden fraction. Assuming that the Si IV resides in a large volume in the MW’s CGM with a radius of 160 kpc, we find a mass of  $\sim 1.6 \times 10^{10} M_{\odot}$  for the hidden CGM and  $\sim 2.3 \times 10^{10} M_{\odot}$  if we add in the high-velocity gas. This is at the lower end of the most recent cool CGM mass estimate from the COS-Halos survey (Prochaska et al. 2017) and is consistent with the value derived in Keeney et al. (2017). Our calculation indicates the MW is likely to host a similarly massive CGM as those  $L^*$  galaxies at low- $z$ ; but we note that the exact number of our mass estimate should be treated with caution given the large uncertainties in the parameter values we have assumed (e.g., ionization fraction and metallicity).

In conducting this study, we perform continuum normalization for a total of 403 QSO spectra observed with HST/COS as released by the HSLA (Peeples et al. 2017). Each co-added spectrum has G130M and/or G160M gratings and has a mean  $S/N \geq 5.0$  over the co-added

wavelength span. Our continuum normalization mainly focuses on interstellar absorption lines, including three ion multiplets S II 1250/1253/1259 Å, Si IV 1393/1402 Å and C IV 1548/1550 Å and other transition lines of P II 1152 Å, C II 1334 Å, Fe II 1142/1143/1144/1608 Å, Si II 1190/1193/1206/1526 Å and Si III 1260 Å. For each QSO we retrieve H I 21cm emission lines from three H I surveys: GALFA-H I (Peek et al. 2017), LAB (Kalberla et al. 2005), and HI4PI (HI4PI Collaboration et al. 2016). The QSO continua, individual line spectra, and the corresponding H I 21cm lines together form our COS-GAL dataset, which we release to the public at [10.17909/T9N677].

In future applications of the COS-GAL dataset, we will study additional ions present in the COS spectra (e.g., the C IV doublet) to address whether the ion excess varies from phase to phase. As our 3D kinematic model is based on SW09’s 1D flat slab, it does not examine any internal structure of the MW’s D/H interface. To explore the internal 3D structure, we will use HST/COS spectra of stars in the MW’s halo at various heights and compare the observed ion column density profiles with the modeled ones. Our COS-GAL dataset has broad potential usage, such as studying the global phenomena of ionized HVCs, gas flows in different directions, the ionized gas properties in specific regions of the MW, or the surroundings of galaxies in the Local Group.

*Acknowledgement.* We thank K. Tchernyshyov for useful discussions on COS ion absorption lines and apparent column density profile derivations. We thank M. Peeples for answering many of our questions about HSLA. We thank S. Flemming for generating the web page to host our COS-GAL dataset as a high-level science product at the Mikulski Archive for Space Telescopes (MAST). We acknowledge support from HST-GO-13706, HST-GO-13383 and HST-GO-13382 which were provided by NASA through grants from the Space Telescope Science Institute (STScI). STScI is operated by the Association of Universities for Research in Astronomy, Inc., under NASA contract NAS5-26555. Most of the data presented in this paper were obtained from the MAST. We also acknowledge support from the National Science Foundation under Grant No. AST-1410800 and AST-1312888. This research made use of the IPython package (Pérez & Granger 2007), matplotlib (Hunter 2007) which is a Python library for publication quality graphics, and Astropy (Astropy Collaboration et al. 2013) which is a community-developed core Python package for Astronomy.

## REFERENCES

Albert, C. E., & Danly, L. 2004, in *Astrophysics and Space Science Library*, Vol. 312, *High Velocity Clouds*, ed. H. van Woerden, B. P. Wakker, U. J. Schwarz, & K. S. de Boer, 73

Asplund, M., Grevesse, N., Sauval, A. J., & Scott, P. 2009, *ARA&A*, 47, 481

- Astropy Collaboration, Robitaille, T. P., Tollerud, E. J., et al. 2013, *A&A*, 558, A33
- Bordoloi, R., Fox, A. J., Lockman, F. J., et al. 2017, *ApJ*, 834, 191
- Bowen, D. V., Jenkins, E. B., Tripp, T. M., et al. 2008, *ApJS*, 176, 59
- Dickey, J. M., & Lockman, F. J. 1990, *ARA&A*, 28, 215
- Dobler, G., Finkbeiner, D. P., Cholis, I., Slatyer, T., & Weiner, N. 2010, *ApJ*, 717, 825
- Ferland, G. J., Korista, K. T., Verner, D. A., et al. 1998, *PASP*, 110, 761
- Ferland, G. J., Porter, R. L., van Hoof, P. A. M., et al. 2013, *RMxAA*, 49, 137
- Fox, A. J., Savage, B. D., & Wakker, B. P. 2006, *ApJS*, 165, 229
- Fox, A. J., Wakker, B. P., Savage, B. D., et al. 2005, *ApJ*, 630, 332
- Fox, A. J., Wakker, B. P., Barger, K. A., et al. 2014, *ApJ*, 787, 147
- Fox, A. J., Bordoloi, R., Savage, B. D., et al. 2015, *ApJL*, 799, L7
- Fraternali, F., & Binney, J. J. 2006, *MNRAS*, 366, 449
- Gnat, O., & Sternberg, A. 2007, *ApJS*, 168, 213
- Haardt, F., & Madau, P. 2001, in *Clusters of Galaxies and the High Redshift Universe Observed in X-rays*, ed. D. M. Neumann & J. T. V. Tran, 64
- Haffner, L. M., Dettmar, R.-J., Beckman, J. E., et al. 2009, *Reviews of Modern Physics*, 81, 969
- HI4PI Collaboration, Ben Bekhti, N., Flöer, L., et al. 2016, *A&A*, 594, A116
- Hunter, J. D. 2007, *Computing In Science & Engineering*, 9, 90
- Joung, M. R., Putman, M. E., Bryan, G. L., Fernández, X., & Peek, J. E. G. 2012, *ApJ*, 759, 137
- Kalberla, P. M. W., Burton, W. B., Hartmann, D., et al. 2005, *A&A*, 440, 775
- Keeney, B. A., Stocke, J. T., Danforth, C. W., et al. 2017, *ApJS*, 230, 6
- Lehner, N., & Howk, J. C. 2011, *Science*, 334, 955
- Lenz, D., Hensley, B. S., & Doré, O. 2017, *ApJ*, 846, 38
- Levine, E. S., Blitz, L., & Heiles, C. 2006, *ApJ*, 643, 881
- Levine, E. S., Heiles, C., & Blitz, L. 2008, *ApJ*, 679, 1288
- Liang, C. J., & Chen, H.-W. 2014, *MNRAS*, 445, 2061
- Martin, C. L., Shapley, A. E., Coil, A. L., et al. 2012, *ApJ*, 760, 127
- Peek, J., Babler, B., Zheng, Y., et al. 2017, Accepted for Publication on *ApJ*
- Peek, J. E. G., Heiles, C., Putman, M. E., & Douglas, K. 2009, *ApJ*, 692, 827
- Peeples, M., Tumlinson, J., Fox, A., et al. 2017, *The Hubble Spectroscopic Legacy Archive*, Tech. rep.
- Pérez, F., & Granger, B. E. 2007, *Computing in Science and Engineering*, 9, 21
- Prochaska, J. X., Werk, J. K., Worseck, G., et al. 2017, *ApJ*, 837, 169
- Putman, M. E., Peek, J. E. G., & Joung, M. R. 2012, *ARA&A*, 50, 491
- Rubin, K. H. R. 2017, in *Astrophysics and Space Science Library*, Vol. 430, *Astrophysics and Space Science Library*, ed. A. Fox & R. Davé, 95
- Rubin, K. H. R., Prochaska, J. X., Koo, D. C., & Phillips, A. C. 2012, *ApJL*, 747, L26
- Rubin, K. H. R., Prochaska, J. X., Koo, D. C., et al. 2014, *ApJ*, 794, 156
- Saul, D. R., Peek, J. E. G., & Putman, M. E. 2014, *MNRAS*, 441, 2266
- Savage, B. D., & Lehner, N. 2006, *ApJS*, 162, 134
- Savage, B. D., & Sembach, K. R. 1991, *ApJ*, 379, 245
- . 1996, *ARA&A*, 34, 279
- Savage, B. D., Sembach, K. R., & Lu, L. 1997, *AJ*, 113, 2158
- Savage, B. D., & Wakker, B. P. 2009, *ApJ*, 702, 1472
- Shull, J. M., Jones, J. R., Danforth, C. W., & Collins, J. A. 2009, *ApJ*, 699, 754
- Stocke, J. T., Keeney, B. A., Danforth, C. W., et al. 2013, *ApJ*, 763, 148
- Tumlinson, J., Peeples, M. S., & Werk, J. K. 2017, *ARA&A*, 55, 389
- Tumlinson, J., Thom, C., Werk, J. K., et al. 2011, *Science*, 334, 948
- van Woerden, H., Wakker, B. P., Schwarz, U. J., & de Boer, K. S., eds. 2004, *Astrophysics and Space Science Library*, Vol. 312, *High Velocity Clouds*
- Wakker, B. P. 1991, in *IAU Symposium*, Vol. 144, *The Interstellar Disk-Halo Connection in Galaxies*, ed. H. Bloemen, 27–40
- Wakker, B. P. 2004, in *Astrophysics and Space Science Library*, Vol. 312, *High Velocity Clouds*, ed. H. van Woerden, B. P. Wakker, U. J. Schwarz, & K. S. de Boer, 25
- Wakker, B. P., Kalberla, P. M. W., van Woerden, H., de Boer, K. S., & Putman, M. E. 2001, *ApJS*, 136, 537
- Wakker, B. P., Savage, B. D., Fox, A. J., Benjamin, R. A., & Shapiro, P. R. 2012, *ApJ*, 749, 157
- Werk, J. K., Prochaska, J. X., Thom, C., et al. 2013, *ApJS*, 204, 17
- Werk, J. K., Prochaska, J. X., Tumlinson, J., et al. 2014, *ApJ*, 792, 8
- Werk, J. K., Prochaska, J. X., Cantalupo, S., et al. 2016, *ApJ*, 833, 54
- Zheng, Y., Peek, J. E. G., Werk, J. K., & Putman, M. E. 2017, *ApJ*, 834, 179
- Zheng, Y., Putman, M. E., Peek, J. E. G., & Joung, M. R. 2015, *ApJ*, 807, 103